KeAi

CHINESE ROOTS
GLOBAL IMPACT

Contents lists available at ScienceDirect

Petroleum Science

journal homepage: www.keaipublishing.com/en/journals/petroleum-science



Original Paper

The role of Cr content on the corrosion resistance of carbon steel and low-Cr steels in the CO₂-saturated brine



Cai-Lin Wang ^{a, b}, Hong-Da Guo ^c, Jian Fang ^d, Sheng-Xian Yu ^d, Xiao-Qi Yue ^e, Qi-Hui Hu ^{a, b}, Cui-Wei Liu ^{a, b, **}, Jia-Xuan Zhang ^f, Rui Zhang ^{a, b}, Xiu-Sai Xu ^{a, b}, Yong Hua ^{d, ***}, Yu-Xing Li ^{a, b, *}

- ^a College of Pipeline and Civil Engineering, China University of Petroleum (East China), Qingdao, Shandong 266580, China
- b Shandong Provincial Key Laboratory of Oil & Gas Storage and Transportation Security, China University of Petroleum (East China), Qingdao, Shandong 266580, China
- ^c School of Materials Science and Engineering, China University of Petroleum (East China), Qingdao, Shandong 266580, China
- ^d Corrosion and Integrity Centre, Zhejiang JIULI Hi-Tech Metals Co., Ltd, Huzhou, Zhejiang 313000, China
- ^e Institute of Advanced Materials and Technology, University of Science and Technology Beijing, Beijing, 100083, China

ARTICLE INFO

Article history: Received 18 January 2022 Received in revised form 14 November 2022 Accepted 21 November 2022 Available online 24 November 2022

Edited by Xiu-Qiu Peng

Keywords: CO₂ corrosion Material selection Cr content CCUS

ABSTRACT

The selection of appropriate materials for the transportation pipelines is of vital importance to ensure the safety operation in Carbon Capture, Utilisation and Storage (CCUS). To clarify the effects of Cr content in steel on the resistance against general and localised corrosion, electrochemistry methods combined with pH measurements and various surface analysis techniques were implemented on X65, 1Cr, 3Cr and 5Cr steel samples in a CO₂-saturated solution at 60 °C and pH 6.6 during 192 h of immersion. Additionally, thermodynamic and kinetic analyses of the formation of the corrosion products on carbon steel and low-Cr steels were performed. The results show that the general corrosion resistance increased with rising Cr content without the presence of significant corrosion products formation. However, with the formation and development of the corrosion products, the general corrosion resistance reduced with the increase in Cr content. The formation of the compact crystalline FeCO₃ on X65 and 1Cr steel surfaces offered superior general corrosion protection, while cannot provide enough localised corrosion protection. By contrast, the double-structural corrosion product layers on 3Cr and 5Cr steels notably suppressed the localised corrosion, but providing poor protection against general corrosion over long immersion periods. This study reveals the contributions of Cr content on general and localised corrosion resistance at various periods, providing references for material selection and evaluation in CO2 environments relevant for CCUS.

© 2022 The Authors. Publishing services by Elsevier B.V. on behalf of KeAi Communications Co. Ltd. This is an open access article under the CC BY-NC-ND license (http://creativecommons.org/licenses/by-nc-nd/4.0/).

1. Introduction

The global climate change causes notable environmental

E-mail addresses: 20180093@upc.edu.cn (C.-W. Liu), leo.huayong@gmail.com (Y. Hua), livx@upc.edu.cn (Y.-X. Li).

problems and is challenging the sustainable development of our society (Sharifzadeh et al., 2019). Carbon Capture, Utilisation and Storage (CCUS) is considered as an important and practical technology to reduce CO₂ emissions and control global warming (Gu et al., 2019; Jiang and Ashworth, 2021; Wang et al., 2019). In the CCUS chain, the captured CO₂ is commonly used for enhanced oil recovery purposes (CO₂-EOR) to achieve economic and effective utilisation and storage (Ajayi et al., 2019; Xu et al., 2020). However, the produced fluids containing oil, water, CO₂ and other substance are corrosive, threatening the integrity of transportation pipelines or wellbores (Hua et al., 2018; Li et al., 2020; Nesic, 2012). Therefore, it is important to select appropriate materials for the

f Pipechina Engineering Technology Innovation Co., Ltd, Tianjin 300000, China

^{*} Corresponding author. College of Pipeline and Civil Engineering, China University of Petroleum (East China), Qingdao, Shandong 266580, China.

^{**} Corresponding author. College of Pipeline and Civil Engineering, China University of Petroleum (East China), Qingdao, Shandong 266580, China.

^{***} Corresponding author. Corrosion and Integrity Centre, Zhejiang JIULI Hi-Tech Metals Co., Ltd, Huzhou, Zhejiang 313000, China.

F-mail addresses: 20180093@unc.edu.cn (C-W. Liu) leo huavong@smail.com

transportation pipelines to ensure the safety operation.

Considering the economic saving, carbon steel material is a popular choice (Cui et al., 2016; Hua et al., 2014; Yang and Yang, 2021). However, its resistance against CO₂ corrosion especially without the formation of the protective corrosion products is weak and can provide a relatively short service life of the pipelines. Previous studies indicate that Cr-containing steels showed better corrosion resistance than carbon steel in CO₂ environments, and the use of 1%–5% Cr steels was able to improve the corrosion resistance of carbon steel and remained the cost within a low limit (Carvalho et al., 2005). Researchers reported that low-Cr alloys such as 3Cr steel were able to improve the CO₂ corrosion resistance significantly and the cost penalty can maintain less than 1.5 times that of the conventional grade of carbon steel (Kermani and Morshed, 2003; Xu et al., 2013).

The corrosion products formed on the surfaces of carbon steel or low-Cr steels can provide certain protection against corrosion, which are regarded as green and cost-effective anti-corrosion films (Hua et al., 2015; Wang et al., 2021). The Cr content in steel has a significant effect on the protective performance of the corrosion product films, influencing the corrosion resistance of the steel materials (Xu et al., 2016). Several studies have been carried out to evaluate the general corrosion behaviours of carbon steel or low-Cr steels as well as the formation of the corrosion products in CO₂ environments. Takabe and Ueda (2001) investigated the corrosion product films and corrosion behaviours of 1Cr, 3Cr and 5Cr steels at 60 °C and CO_2 partial pressure (p_{CO_2}) of 3 MPa, and it was found that 3Cr and 5Cr steels showed better corrosion resistance than 1Cr steel. Bai et al. (2006) used electrochemical impedance spectroscopy (EIS) to compare the corrosion resistance of 4Cr and N80 steels in CO₂ environments, and the protective performance of the corrosion products on 4Cr steel was found to be better than that of N80 steel. The research by Xu et al. (2016) investigated the corrosion behaviours of 1–6.5Cr steels at 80 °C and p_{CO_2} of 0.8 MPa with a duration of 120 h, and the results indicated that general corrosion rate reduced with the improvement in Cr content. They pointed out that an adequate amount of Cr content in steel resulted in the precipitation of Cr(OH)₃ layer, which led to prepassivation characteristics and improved general corrosion resistance. Guo et al. (2012) compared X65, 1Cr, 2Cr and 3Cr steels in CO2 environments at 80 °C and 0.8 MPa p_{CO_2} . Two corrosion products layers were observed, the outer layer of FeCO₃ crystals grew on the inner layer of Cr(OH)₃ on the 3Cr steel surface. They also mentioned that the Cr content can influence the pH value then affect the formation of the corrosion products. Zhao et al. (2020) studied the corrosion behaviours of 1Cr, 3Cr, 5Cr and 9Cr in CO₂ environments with the addition of silty sand, and they found that the rise in Cr content improved the protectiveness of the passive film, leading to a better general corrosion resistance of Cr alloy steels. Moreover, Sun et al. (2021) found that the increase in Cr content can improve general corrosion resistance of low-Cr steels in a simulated tropical marine atmosphere that the formation of the Cr₂O₃ and Cr(OH)₃ films can offer corrosion protection to the surface. Clearly, most previous studies indicate that the increase in Cr content can enhance the general corrosion resistance of Cr-containing steels. However, there are also some researchers finding that the Cr content could have different effects on general corrosion resistance. Sun et al. (2020) evaluated the corrosion resistance of Cr-containing steels in an atmospheric environment and the results showed that the general corrosion rate did not change in the range of 1%-4% Cr content. Hua et al. (2020) evaluated the corrosion behaviours of X65, 1Cr, 3Cr and 5Cr steels in CO₂ environments at 60 °C and 10 MPa, and the results indicated that the Cr content had a significant effect on the formation of the corrosion products which influenced the corrosion resistance of the steels. The general corrosion resistance increased

with rising Cr content without precipitation of the corrosion products, however, as the corrosion products evolved, X65 steel showed the best corrosion resistance against general corrosion after 192 h. In addition, the morphology and protectiveness of the corrosion product scales on X70 and 3Cr steels were compared in a CO_2 — O_2 coexistent environment after pure CO_2 corrosion by Chen et al. (2022), and the general corrosion rate of 3Cr steel was found to be much higher than that of X70 steel in the first 24 h due to the porous structure and the hydrolysis of $Cr(OH)_3$.

In respect of the localised corrosion, Chen et al. (2005) investigated the localised corrosion and the corrosion products on 1Cr, 4Cr and N80 steels in CO₂ environments. The results indicated that the low-Cr steels could resist localised corrosion effectively. They also found that the Cr(OH)₃ content increased significantly in corrosion products with increasing Cr content which could protect the steel against pitting corrosion. The work of Xie et al. (2012) showed similar findings that 3Cr steel had a better localised corrosion resistance than X70 carbon steel due to the inner Cr-enriched layer on 3Cr surfaces. However, the study by Hua et al. (2020) suggested that increasing Cr content was not able to improve localised corrosion resistance.

Based on the previous studies, it remains unclear for the role of Cr content on the formation and anti-corrosion properties of the corrosion products, especially the effects of Cr content on localised corrosion resistance of steels. It is highly required to reveal the formation kinetics of the corrosion product films and their protectiveness against corrosion for the steels with different Cr contents, then explain the relationship between Cr content and corrosion resistance of steels at various corrosion periods.

This article intends to clarify the effects of Cr content on the general and localised corrosion resistance of steels at various immersion times. The precipitation of the corrosion products and their evolution on X65, 1Cr, 3Cr and 5Cr steels were systematically compared using a combination of scanning electron microscopy (SEM), X-ray diffraction (XRD) and Raman spectroscopy. The electrochemistry methods such as EIS, linear polarisation resistance (LPR) and polarisation curves, combined with surface profilometry were implemented to determine the extent of general and localised corrosion. The evolutions of active surface areas on different steels were also calculated based on the electrochemical measurements to further analyse the anti-corrosion properties of the corrosion products. Moreover, pH measurements of the solution near the steel surface were conducted to supplement the corrosion process and formation mechanism of the corrosion products.

2. Materials and methods

2.1. Materials and solution

In this study, X65, 1Cr, 3Cr and 5 Cr steels were evaluated by electrochemistry measurements and immersion tests. The chemical compositions and microstructures of those steels are provided in Table S1 and Fig. S1, respectively. It can be noted that the ferrite-pearlite microstructures were observed on X65 carbon steel. For 1Cr steel, inhomogeneous distribution of martensite and ferrite was found. Randomly distributed carbides were seen on 3Cr steel, while carbides in ferrite matrix were demonstrated on 5Cr steel.

The samples for electrochemistry tests and immersion tests were sectioned into discs of diameter 25 mm and thickness 6 mm. Conductive wires were soldered to the back of each sample and then embedded in a non-conducting resin for electrochemistry experiments. Similarly, each sample was embedded in a resin for immersion tests. It should be noted that only one circular surface was exposed to the electrolyte for both electrochemistry measurements and immersion experiments, thus the total exposure

area was 4.9 cm². Prior to the experiments, samples were wet ground up to 600 grit by using silicon carbide paper, washed with acetone and distilled water, then dried with compressed air.

According to the literature, the pH value of the produced fluids by CO₂ flooding at the wellhead can be approximately 7 (Yan et al., 2015). To simulate the produced fluids environments, 1 L CO₂-saturated 3 wt% NaCl brine with the addition of 0.5 wt% NaHCO₃ was used as the test solution. Both the electrochemistry tests and immersion tests were conducted at 60 °C and $p_{\rm CO_2}$ 0.8 bar. The test conditions are summarised in Table 1. The $p_{\rm CO_2}$ and the initial pH values were calculated via the OLI software (OLI Systems, Inc). The test solution was bubbled with CO₂ for 12 h prior to each test in order to remove oxygen from the system. All tests have been repeated a minimum of three times.

2.2. Electrochemistry tests

Electrochemistry experiments were performed using a standard three-electrode cell system, as shown in Fig. S2(a). The vessel was sealed, and CO_2 was continuously bubbled into the solution to ensure complete CO_2 saturation throughout the test.

In the three-electrode system, an Ag/AgCl electrode in a saturated KCl solution was used as the reference electrode, and the counter electrode is a platinum. The measured Ag/AgCl reference electrode potentials in our experiments were converted into standard hydrogen electrode (SHE) potentials according to the following relationship (Macdonald et al., 1979):

$$\begin{split} E_{\text{SHE}} \!=\! E_{\text{Ag/AgCl}} \!+\! 0.2866 \!-\! 0.001 (T \!-\! T_0) \!+\! 1.754 \!\times\! 10^{-7} (T \!-\! T_0)^2 \\ \!-\! 3.03 \times 10^{-9} (T \!-\! T_0)^3 \end{split}$$

where $E_{\rm SHE}$ is the SHE electrode potential, $E_{\rm Ag/AgCl}$ is the Ag/AgCl reference electrode potential, T is the test temperature and T_0 is the reference temperature (25 °C).

LPR measurements were carried out from -15 mV vs. open circuit potential (OCP) to +15 mV vs. OCP at a scan rate of 0.167 mV/s to determine the polarisation resistance measurement (R_p). The corrosion current density i_{corr} can be calculated from polarisation resistance (R_p) using Eq. (2):

$$i_{\text{corr}} = \frac{B}{R_{\text{p}}} = \frac{\beta_{\text{a}}\beta_{\text{c}}}{2.303R_{\text{p}}(\beta_{\text{a}} + \beta_{\text{c}})}$$
 (2)

where β_a and β_c are the anodic and cathodic Tafel constants, respectively. In this study, $1/R_p$ was used to represent the instantaneous general corrosion rate semi-quantitatively. Anodic and cathodic sweeps were conducted separately in Tafel polarisation measurements. Scans started at OCP and extended ± 500 mV at a scan rate of 0.167 mV/s. For EIS tests, the frequency range was from 100 kHz to 1 mHz with an amplitude perturbation of 10 mV. To fit the measured EIS results, equivalent electrical circuits were applied with fitting errors <10%.

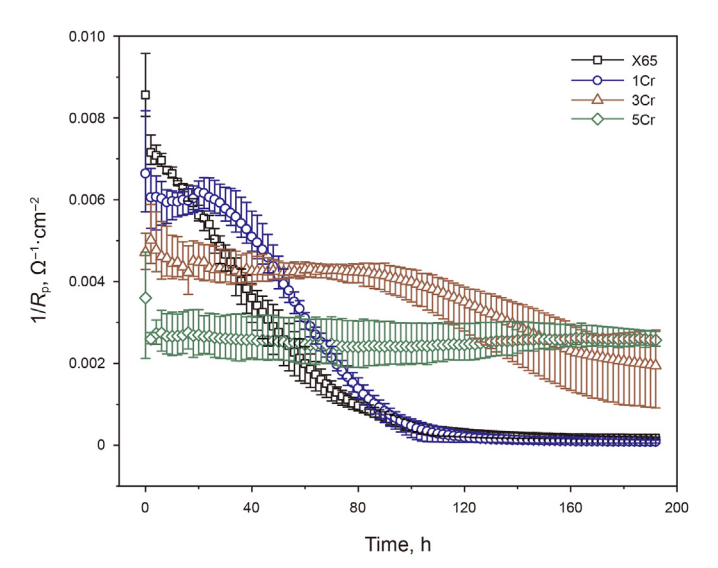


Fig. 1. Variations of $1/R_p$ for X65, 1Cr, 3Cr and 5Cr steels exposed to CO_2 -saturated NaCl solution during 192 h by LPR measurements.

2.3. pH measurements

As displayed in Fig. S2(b), the steel sample was suspended upward and a pH probe was set close to the steel surface. The pH values of the solution near the steel surfaces were monitored during the immersion tests by a pH meter (pHS-2F, LEICI Instruments, China).

2.4. Surface analysis

(1)

SEM, XRD and Raman spectroscopy were used to characterise the morphology and chemical composition of the corrosion products on the steel surfaces.

To determine the localised attacks, the corrosion products were removed from the steel surfaces by using Clark's solution according to ASTM Standard G1-03 (ASTM, 2003a). Then surface profilometry measurements were performed. Three random areas and each area with a total area of 3×3 mm² were scanned at a time. Referring to ASTM Standard G46-94 (ASTM, 2003b), an average of the 10 deepest pits from three samples was considered for the localised/pitting attack analysis in each condition.

3. Results

3.1. General corrosion behaviours of different steels at various immersion times

The $1/R_p$ results by LPR measurements for X65, 1Cr, 3Cr and 5Cr samples exposed to CO₂-saturated solution at pH 6.6 and 60 °C over 192 h are shown in Fig. 1. For X65 steel, the highest $1/R_p$ value of approximately 0.0085 Ω^{-1} cm⁻² was observed at the initial stage due to the fast iron dissolution and then decreased with exposure times. The $1/R_p$ reduced significantly for X65 and 1Cr steels, both

Table 1Test conditions for corrosion tests.

Temperature, °C	Total pressure, bar	p_{CO_2} , bar	Solution	Solution pH (±0.05)	Materials	Immersion time, hours
60	1	0.8	3 wt% NaCl + 0.5 wt% NaHCO ₃	6.64	X65/1Cr/3Cr/5Cr	6/24/48/96/192

reaching nearly 0 Ω^{-1} cm⁻² after 192 h. For 3Cr steel, the $1/R_p$ value reduced slowly to 0.002 Ω^{-1} cm⁻² after 192 h. For 5Cr, the $1/R_p$ stabilised at 0.0025 Ω^{-1} cm⁻² during the 192 h of immersion tests. Clearly, the general corrosion rates of different materials reduced with rising Cr content in the absence of protective corrosion products during the initial period. However, with the development of the corrosion products, the corrosion resistance of different materials reduced with Cr content because the corrosion product layers on X65 and 1Cr surfaces were protective, while the corrosion product layers on 3Cr and 5Cr offered poor protectiveness against general corrosion.

3.2. Formation and evolution of the corrosion product layers

Figure 2 shows the top-view morphologies for the corrosion products developed on different steel surfaces after 24 h. More surface morphologies of different steels after various immersion periods are provided in Figs. S3 and S4. It is clear that crystals precipitated on the X65 and 1Cr surfaces after 6 h as presented in Fig. S3 (a and c) and almost covered the entire surfaces after 24 h as shown in Fig. 2 (a and b). No crystals were observed on 3Cr and 5Cr surfaces after 24 h, suggesting that the growth of crystals can be delayed by the addition of Cr content in the steel at the initial 24 h.

Surface morphologies of the four steel samples after 96 h are displayed in Fig. 3. Clearly, a full coverage of the corrosion products was achieved on X65 and 1Cr steel surfaces after 96 h. For 3Cr and 5Cr steels, the SEM images indicated the crystalline film coverage became less as increasing Cr content and the corrosion products comprised of a double-layer structure. The crystal layer was precipitated on the inner amorphous layer after 96 h.

Figure 4 shows the cross-sections SEM images of the corrosion product layers formed on different steels by the end of 192 h. It is clear that a uniform corrosion product layer with a thickness of approximately 10 μ m was recorded for X65, 1Cr and 3Cr steels. The thickness of the corrosion product layer was relatively less uniform for 5Cr and was agreed with the observed crystals from the top

view SEM image provided in Fig. S4(h) that the crystals were randomly distributed on the 5Cr steel surface.

The XRD patterns for X65 and 5Cr steels after various exposure times are displayed in Fig. 5. The XRD results indicated only FeCO₃ crystals were observed on each exposure time. It is interesting to note that no Cr-containing corrosion products were identified by XRD, suggesting that the Cr-rich layer was mainly amorphous or it was a nanoparticle layer which cannot be detected by XRD.

Raman spectroscopy was employed to further characterise the inner corrosion product layers on 3Cr and 5Cr steels after 192 h. As illustrated in Fig. 6(c), the peaks located at 290, 743 and 1086 cm $^{-1}$ were identified as FeCO $_3$ and the peak for the presence of Cr(OH) $_3$ was confirmed at 715 cm $^{-1}$. The work of Xu et al. (2016) reported the same observation of the inner amorphous layer was mainly Cr(OH) $_3$ for different Cr steels in CO $_2$ -saturated formation water. Additionally, Guo et al. (2012) performed the tests for 2Cr steel in a CO $_2$ -saturated solution, and the double corrosion product layers were identified as an inner amorphous Cr(OH) $_3$ layer and an outer crystalline FeCO $_3$ layer.

3.3. Polarisation curves of different steels on the early and final formations

Figure 7(a) shows the Tafel plots for different steels exposed to CO_2 -saturated solution at 60 °C and pH 6.6 after 6 h. The corrosion potentials (E_{corr}) showed unchanged with increasing Cr contents (approximately -0.7 V vs. Ag/AgCl) and the cathodic curves with no obvious change in the shape. However, a clearly prepassivation (Region AB) can be observed on the anodic reaction with the increase in Cr contents and this prepassivation disappeared for X65, suggesting that the prepassivation was attributed to the formation of the Cr-rich corrosion product layer on the surfaces of 1Cr, 3Cr and 5Cr samples. Additionally, the anode polarisation curves shifted to the left with the increase of Cr content, in consistent with the research by Xu et al. (2016). The values of E_{corr} and E_{corr} as well as the Tafel slopes for X65, 1Cr, 3Cr and 5Cr materials after 6 h are listed in

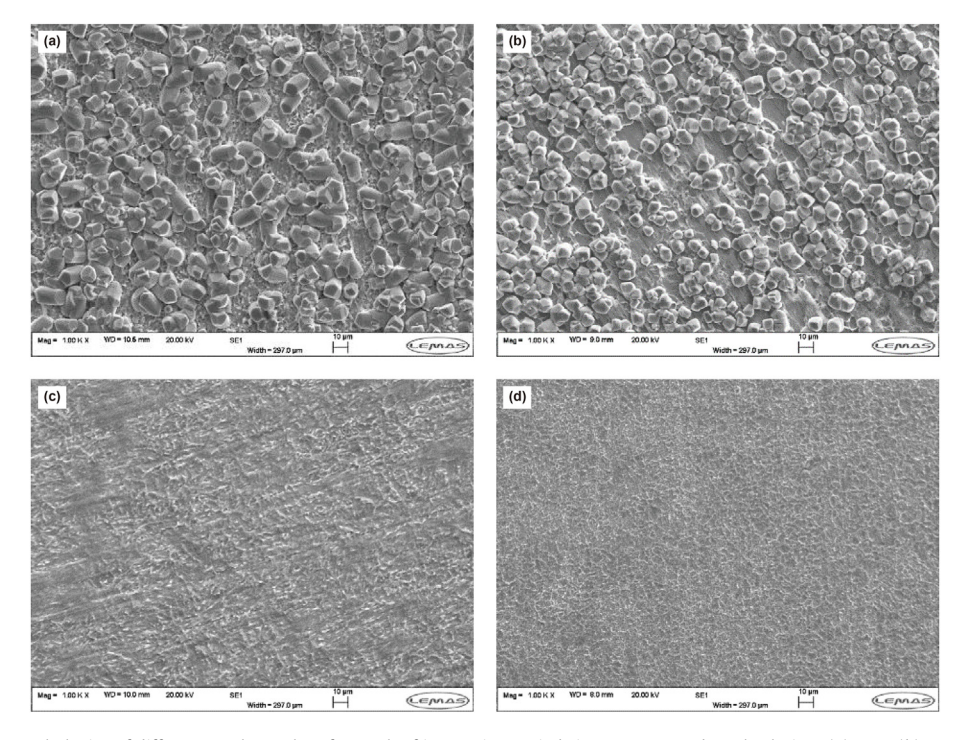


Fig. 2. Surface morphologies of different steel samples after 24 h of immersion periods in CO₂-saturated NaCl solution: (a) X65; (b) 1Cr; (c) 3Cr; (d) 5Cr.

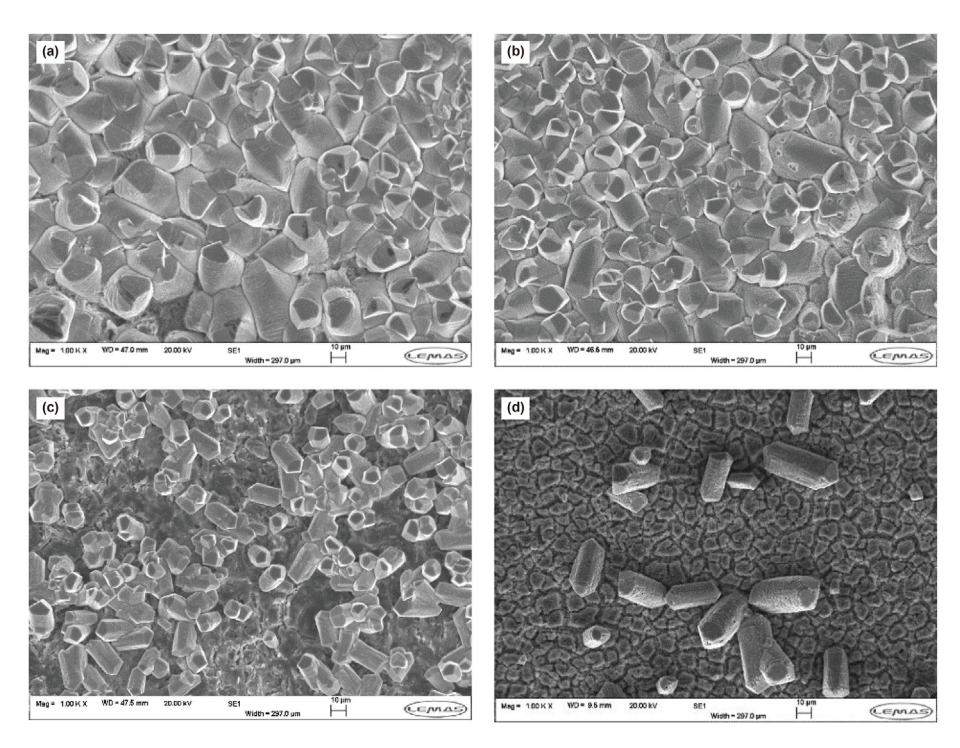


Fig. 3. Surface morphologies of different steel samples after 96 h of immersion periods in CO₂-saturated NaCl solution: (a) X65; (b) 1Cr; (c) 3Cr; (d) 5Cr.

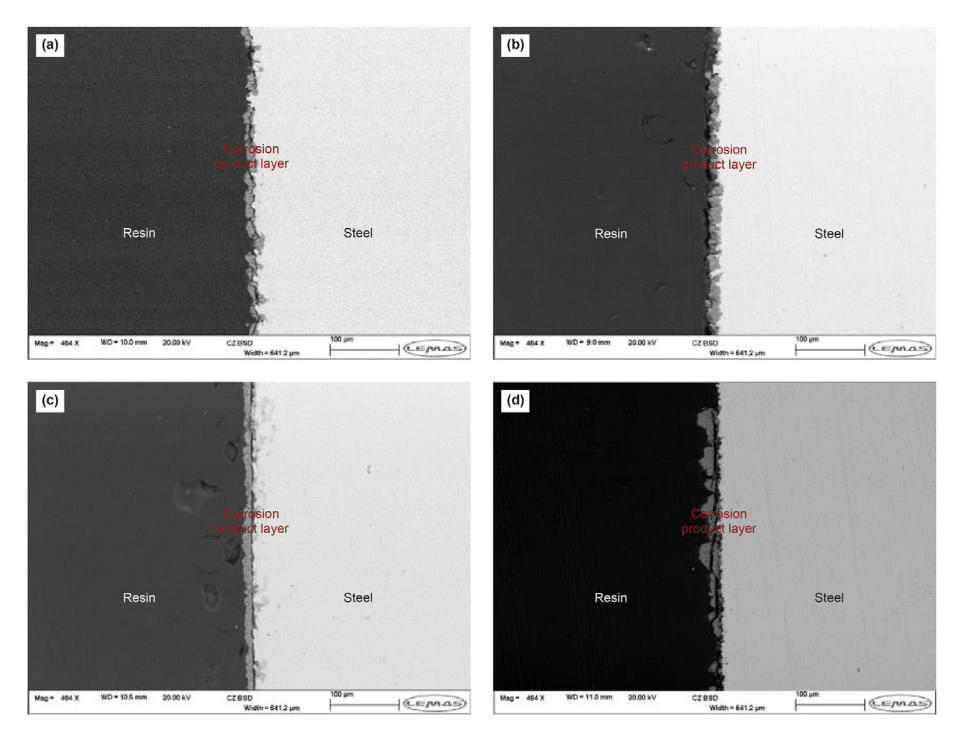


Fig. 4. Cross-section SEM images of different steel samples exposed to the CO₂-saturated NaCl solution after 192 h: (a) X65; (b) 1Cr; (c) 3Cr and (d) 5Cr.

Table S2. Clearly, the $i_{\rm corr}$ reduced with increasing Cr content, with the highest of 0.65 mA/cm² for X65 and the lowest of 0.18 mA/cm² for 5Cr, confirming that the general corrosion resistance was improved with the increase in Cr content at the initial corrosion stage.

The Tafel polarisation plots for the four steels after 192 h of exposure are displayed in Fig. 7(b). Compared with the polarisation curves after 6 h, $E_{\rm corr}$ exhibited negligible changes for 3Cr and 5Cr

steels after 192 h, while $E_{\rm corr}$ increased from -0.7 V to approximately -0.61 V and -0.65 V, for X65 and 1Cr steel, respectively. In addition, both the anodic and cathodic polarisation curves for the four steels shifted to the left, indicating the decreased corrosion current density ($i_{\rm corr}$). The left-shifts of the polarisation curves for X65 and 1Cr were more significant than 3Cr and 5Cr, suggesting better corrosion resistance of the X65 and 1Cr samples after 192 h.

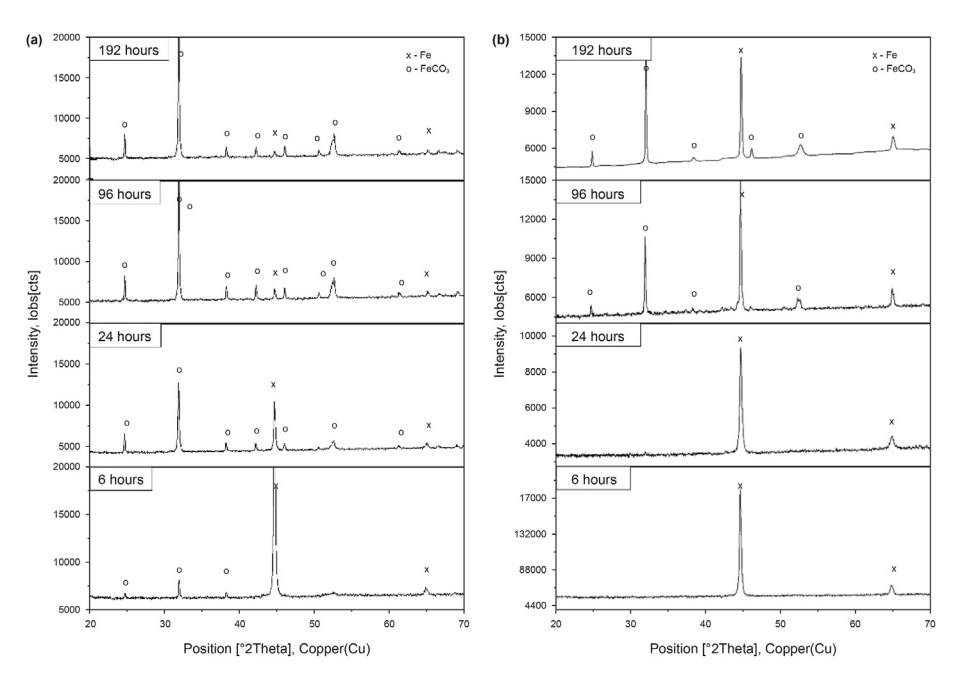
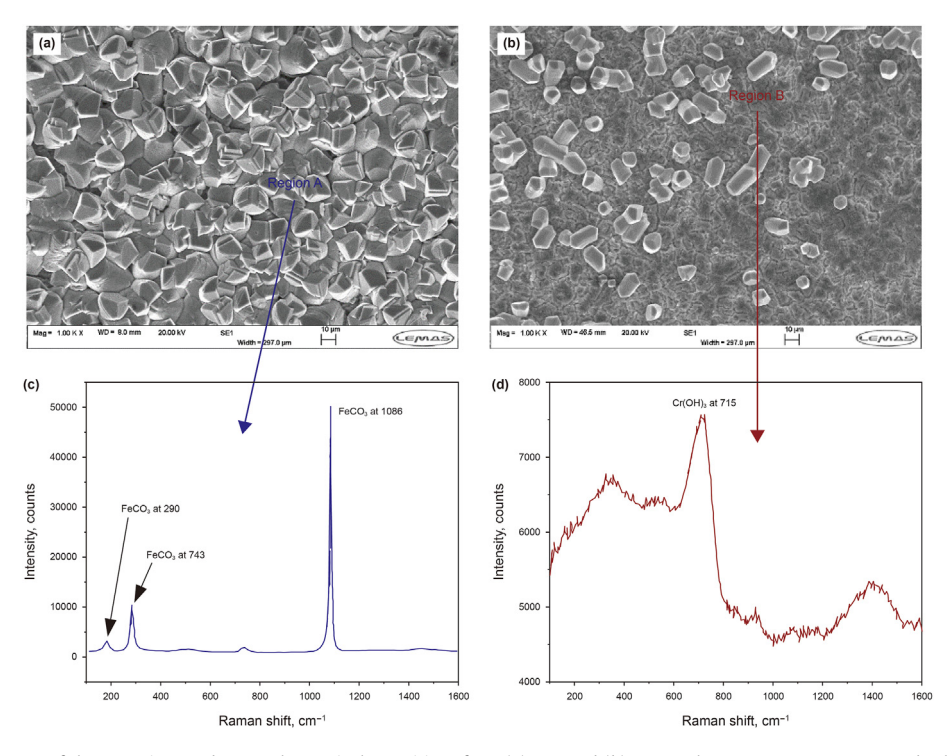


Fig. 5. XRD patterns of (a) X65 carbon steel and (b) 5Cr steel exposed to the CO₂-saturated solution after 6, 24, 96 and 192 h.



 $\textbf{Fig. 6.} \ \ \text{Raman spectra of the corrosion products at the particular positions from (a) X65 \ \text{and (b) 5Cr steels exposure to CO}_2\text{-saturated solution after 192 h.}$

In addition, great differences were observed on the shapes of the anodic curves between X65/1Cr and 3Cr/5Cr after 192 h of exposure. Referring to the literature (Guo et al., 2016), a series of passivation (CD) and transpassivation (DE) phenomena were found for X65 and 1Cr steels from Fig. 7(b). The passivation region was due to the growth of the corrosion product film on the metal surface, and the lowest passivation current density was recorded for X65, indicating a more compact structure of the corrosion product layer on X65 steel surface. At the transpassivation region, the current density increased which was possibly related to the local

breakdown of the corrosion product layer. By contrast, the Tafel plots for 3Cr and 5Cr after 192 h were similar to those after 6 h, and only passivation (GH) was observed, suggesting a relatively porous structure and poor protectiveness of the corrosion product film on steel surfaces (Guo et al., 2016).

3.4. EIS analysis on different steels at various immersion times

Figure 8 shows the Nyquist and Bode plots of different samples after 6 h, 24h, 96 h and 192 h immersion times. For the X65 and 1Cr

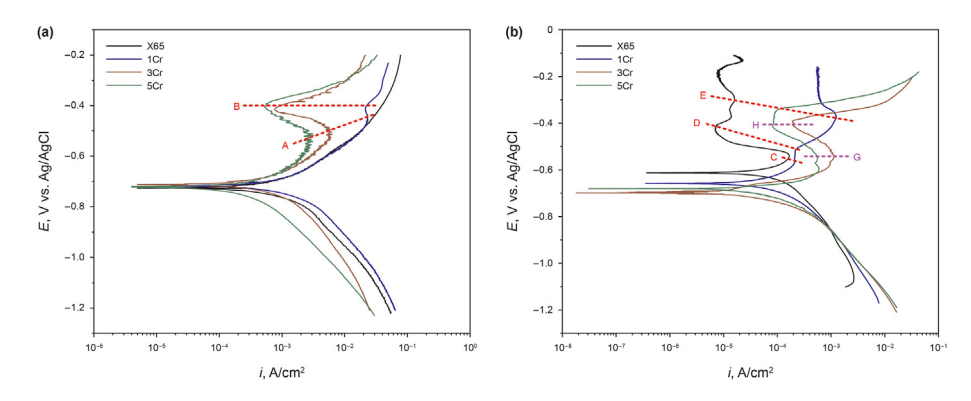


Fig. 7. Tafel polarisation plots for X65, 1Cr, 3Cr and 5Cr steels after (a) 6 h and (b) 192 h exposure.

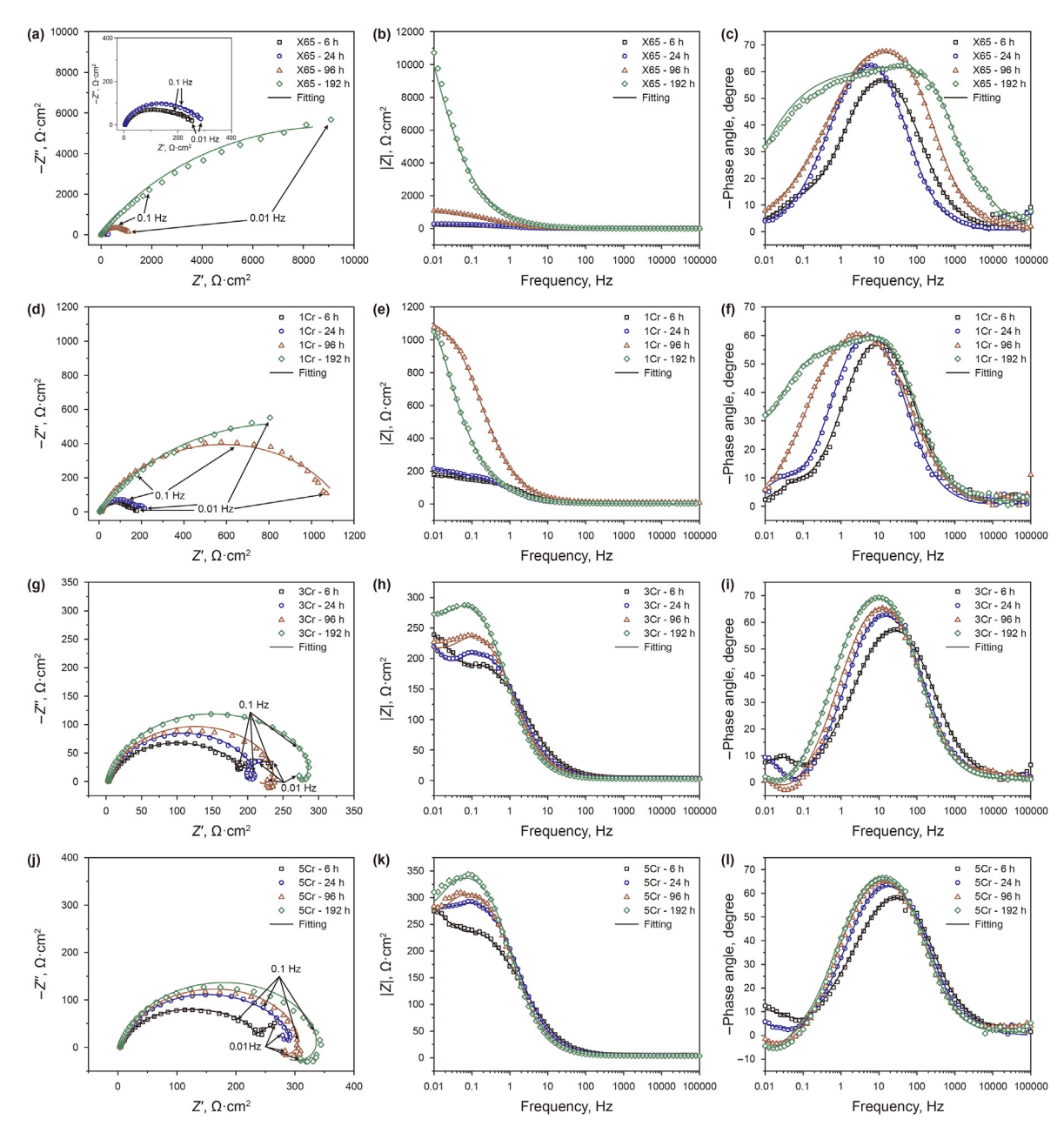


Fig. 8. Nyquist plots of the (a) X65, (d) 1Cr, (g) 3Cr and (j) 5Cr steels and Bode plots of the (b, c) X65, (e, f) 1Cr, (h, i) 3Cr and (k, l) 5Cr steels after various immersion times in CO₂-saturated NaCl solution.

materials, two responses were identified from the Nyquist diagrams and Bode diagrams during the 192 h of exposure: a capacitive response from high frequency (HF) to medium frequency (MF) range and a capacitive response in low frequency (LF) range. The HF-MF response was related to the precipitation the corrosion product scales, in consistent with the SEM observations in Fig. S3 where FeCO₃ crystals were formed on the top surfaces of the X65 and 1Cr samples after 6 h. The LF capacitive semicircle was due to the charge transfer process at the interface between the substrate and solution.

As displayed in the Nyquist plots, the amplitude of the HF-MF capacitive semicircle increased with exposure time for X65 and 1Cr steels, and the corresponding Bode phase angle plots showed the peak at MF which rose with time, indicating a growing protectiveness of the corrosion products, in agreement with SEM observations that denser crystalline FeCO₃ corrosion products were formed on X65 and 1Cr surfaces with immersion time. It should be noted that there was a significant increase in the amplitude in impedance results after 96 h because the steel surface was almost fully covered with compact FeCO₃ crystals at that time, as displayed in Fig. 3. Additionally, the maximum at LF in the phase angle plots and the corresponding modulus of the impedance increased with time, which was related to the increase of the charge transfer resistance, as the continuous precipitation of FeCO₃ blocked charge transfer sites on the steel surfaces.

Different from the impedance results of X65 and 1Cr samples, the Nyquist plots of the 3Cr and 5Cr samples showed three responses during the 192 h of immersion tests: an HF-MF capacitive semicircle, an LF capacitive semicircle and an inductive semicircle. The HF-MF capacitive loop represented the corrosion product films on the metal surface, and the LF capacitive loop characterised the state of the interfacial electric double layer. The inductive semicircle in the LF range was attributed to the dynamic adsorption of intermediate products on the steel surfaces (Li et al., 1996) according to the following reactions:

$$Fe + H_2O \rightleftharpoons FeOH_{ads} + H^+ + e^-$$
 (3)

$$FeOH_{ads} \rightarrow FeOH_{sol}^{+} + e^{-} \tag{4}$$

$$FeOH_{sol}^{+} + H^{+} \rightleftharpoons Fe_{sol}^{2+} + H_{2}O$$
 (5)

$$Cr + H_2O \rightleftharpoons CrOH_{ads} + H^+ + e^-$$
 (6)

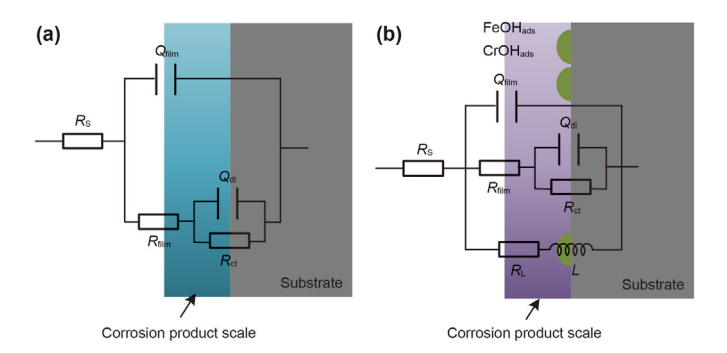
$$CrOH_{ads} \rightarrow CrOH_{sol}^{+} + e^{-} \tag{7}$$

$$CrOH_{sol}^{+} + H^{+} \rightleftharpoons Cr_{sol}^{3+} + H_{2}O + e^{-}$$
 (8)

According to the research of Zhu et al. (2015), there were three stages in the corrosion process for 3Cr steel: dynamic adsorption, incomplete-coverage layer formation and integral layer formation. The above adsorptions of FeOH_{ads} and CrOH_{ads} occur on the substrate surfaces in the initial stage, and the sign of the integral layer formation is the disappearance of the LF inductive loop. Clearly, the LF inductive loop was observed during the whole 192 h of exposure for the 3Cr and 5Cr steels, thus the integral layer had not been formed within 192 h on the 3Cr and 5Cr steels in our research, which agrees with Li's study (Li et al., 2017) that the LF inductive semicircle can maintain for 240 h for the 3Cr steel at 80 °C and $p_{\rm CO_2}$ of 0.8 MPa. As shown in Fig. 2, no obvious crystalline corrosion products were observed on the 3Cr steel surfaces after 24 h of exposure, and the 3Cr and 5Cr steel surfaces were locally covered with FeCO₃ crystals after 192 h. Though Cr(OH)₃ was identified

under the FeCO₃ crystals, the Cr(OH)₃ cannot offer enough protection as the general corrosion rates remained high from the LPR results. As a result, there were exposed steel surface areas to the electrolyte to provide sites for the dynamic adsorption of the FeOH_{ads} and CrOH_{ads} on the 3Cr and 5Cr surfaces. Notably, the inductive response was not present for the X65 and 1Cr samples which was attributed to the massive corrosion product precipitation on the metal surface. Additionally, only slight increases were observed on the amplitude of the HF-MF capacitive semicircle for the 3Cr and 5Cr steels, suggesting a poor protectiveness of the corrosion products on the 3Cr and 5Cr surfaces. As shown in the Bode plots of the 3Cr and 5Cr samples, the peak with maximum phase angle increased and shifted to low frequency with the exposure time, which was correlated to the growth of the corrosion product layer.

To further analyse the EIS results, equivalent circuits were applied for the four steels after various exposure times. The equivalent circuit in Fig. 9(a) was applied to characterise the impedance spectra of X65 and 1Cr after 6 h–192 h, where $R_{\rm S}$ is the solution resistance, $Q_{\rm film}$ is the constant phase element (CPE) describing the corrosion product layer, $R_{\rm film}$ is the resistance of the layer, $Q_{\rm dl}$ is the CPE which represents the double layer capacitance, $R_{\rm ct}$ is the charge transfer resistance. The CPE element was used for considering the dispersion effect or surface inhomogeneity, and the CPE ($Z_{\rm CPE}$) is defined by:



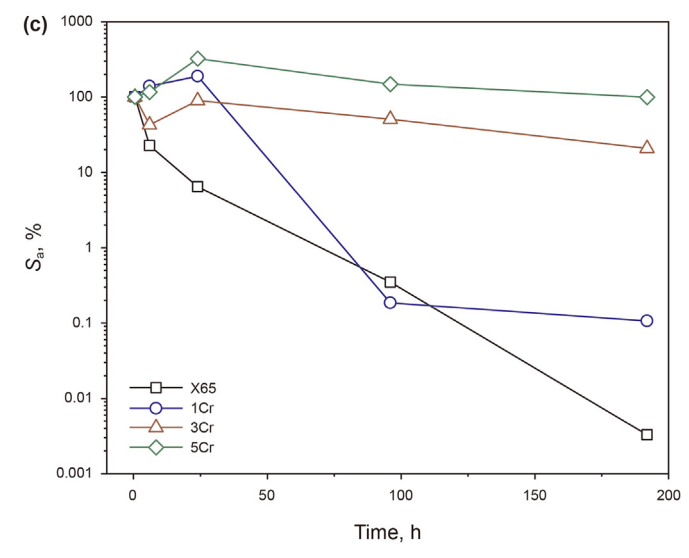


Fig. 9. Equivalent circuits to fit the EIS results and the calculated S_a results: (a) equivalent circuit for X65 and 1Cr samples; (b) equivalent circuit for 3Cr and 5Cr samples; (c) S_a values for the four steels after different immersion times.

$$Z_{\text{CPE}} = \frac{1}{Q(j\omega)^n} \tag{9}$$

where Q is the proportional factor, $j=\sqrt{-1}$, $\omega=2\pi f$, and n is the factor which takes values between 0 and 1. The equivalent circuit displayed in Fig. 9(b) was applied to fit the impedance results of the 3Cr and 5Cr samples, where $R_{\rm L}$ is the inductive resistance and L is the inductance. The fitted results are displayed in Fig. 8 and the fitted parameters are listed in Table S3. It can be seen from Table S3 that the fitted $R_{\rm Ct}$ parameters of the X65 and 1Cr steels increased dramatically with immersion time, confirming the decrease of general corrosion rates.

The double layer capacitance C_{dl} can be determined by the Brug's equation (Brug et al., 1984):

$$C_{\rm dl} = Q_{\rm dl}^{\frac{1}{n}} \left(\frac{R_{\rm s} R_{\rm ct}}{R_{\rm s} + R_{\rm ct}} \right)^{\frac{1-n}{n}} \tag{10}$$

Assuming the physical and chemical conditions are constant on the bare substrate surfaces, the fraction of active surface area (S_a) can be calculated using Eq. (11) (Motte et al., 2020):

$$S_{\rm a}\%(t) = \frac{C_{\rm dl}(t)}{C_{\rm dl}(0)} \times 100\%$$
 (11)

where $S_a\%(t)$ represents the S_a fraction at time t; $C_{\rm dl}(t)$ is the double layer capacity at time t and $C_{\rm dl}(0)$ is the double layer capacity at the initial immersion time. In our study, the double layer capacity after 0.5 h of exposure was applied as the $C_{\rm dl}(0)$.

The variations of S_a with exposure times for the four steels are shown in Fig. 9(c). Clearly, the S_a tended to decline dramatically for the X65 and 1Cr steels. The S_a reduced from 100% to below 1% after 96 h of immersion for both X65 and 1 Cr steels, indicating that the steel surface had been blocked by the FeCO₃ corrosion products, which was in consistent with the SEM observations and LPR results. For 3Cr steel, the S_a declined to 21% after 192 h, showing a weaker protective performance of the double layer corrosion product films and the metal surface was only partially blocked by the corrosion products. It is worth noting that the calculated S_a values for 5Cr rose notably to nearly 400% after 24 h, then decreased to approximately 100% after 192 h, confirming that the corrosion product film offered little protectiveness on the steel surface under the current experimental conditions, agreeing with the LPR measurements. Furthermore, the S_a results suggest that the inner structure of FeCO₃ was more compact and tightly adherent to the steel surfaces than the double FeCO₃ and Cr(OH)₃ layer in our experimental environments, though the thicknesses of both were similar as shown in Fig. 4.

Time. h

3.5. Localised corrosion measurements

Figure 10 indicates the localised depths and the localised corrosion rates for different steels immersed in the CO_2 -saurated brine at 60 °C and pH 6.6 for various times. The examples of profilometry images for those samples after 192 h are provided in Fig. 11.

For all the four materials, the results show that the localised corrosion depth increased with time, indicating that the localised attack continued to propagate during the overall 192 h. The compact and dense FeCO $_3$ layer formed on the X65 and 1Cr surfaces can reduce the general corrosion rate, however this layer did not provide enough protection for the localised corrosion. The highest localised depth reached 25 μ m for 1Cr steel after 192 h, by contrast, 3Cr and 5Cr exhibited the lowest pitting depth at 15 μ m after 192 h. As the corrosion products evolved, the highest localised corrosion rated was 1.17 mm/year for 1Cr after 192 h, while the localised corrosion rates for 3Cr and 5Cr were the lowest, approximately 0.66 mm/year by the end of 192 h, indicating that the corrosion product layers on 3Cr and 5Cr steels provided superior protectiveness against localised corrosion.

Clearly, less localised attacks were observed for 3Cr and 5Cr during the 192 h immersion tests, and 5Cr steel showed the best localised corrosion resistance. This work shows that the increasing the Cr content to 3Cr is able to increase the localised corrosion resistance despite of the development of corrosion products under the test condition here.

4. Discussion

4.1. Formation mechanism of the corrosion products on different steels in CO_2 environments

The CO₂-saturated NaCl solution produces carbonic acid and then becomes bicarbonate and carbonate ions as shown in the following reactions:

$$CO_{2(g)} \rightleftharpoons CO_{2(aq)} \tag{12}$$

$$CO_{2(aq)} + H_2O_{(l)} \rightleftharpoons H_2CO_{3(aq)}$$

$$\tag{13}$$

$$H_2CO_{3(aq)} \rightleftharpoons HCO_{3(aq)}^- + H_{(aq)}^+$$

$$\tag{14}$$

$$HCO_{3(aq)}^{-} \stackrel{.}{=} CO_{3(aq)}^{2-} + H_{(aq)}^{+}$$
 (15)

The anodic reactions include the dissolutions of iron and chromium:

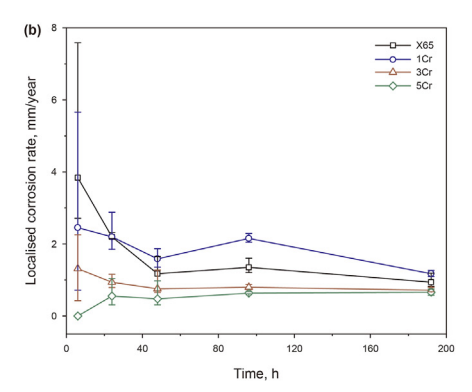


Fig. 10. Measured (a) pit depths and (b) localised corrosion rates for X65, 1Cr, 3Cr and 5Cr steels exposed to CO₂-saturated solution after various immersion times.

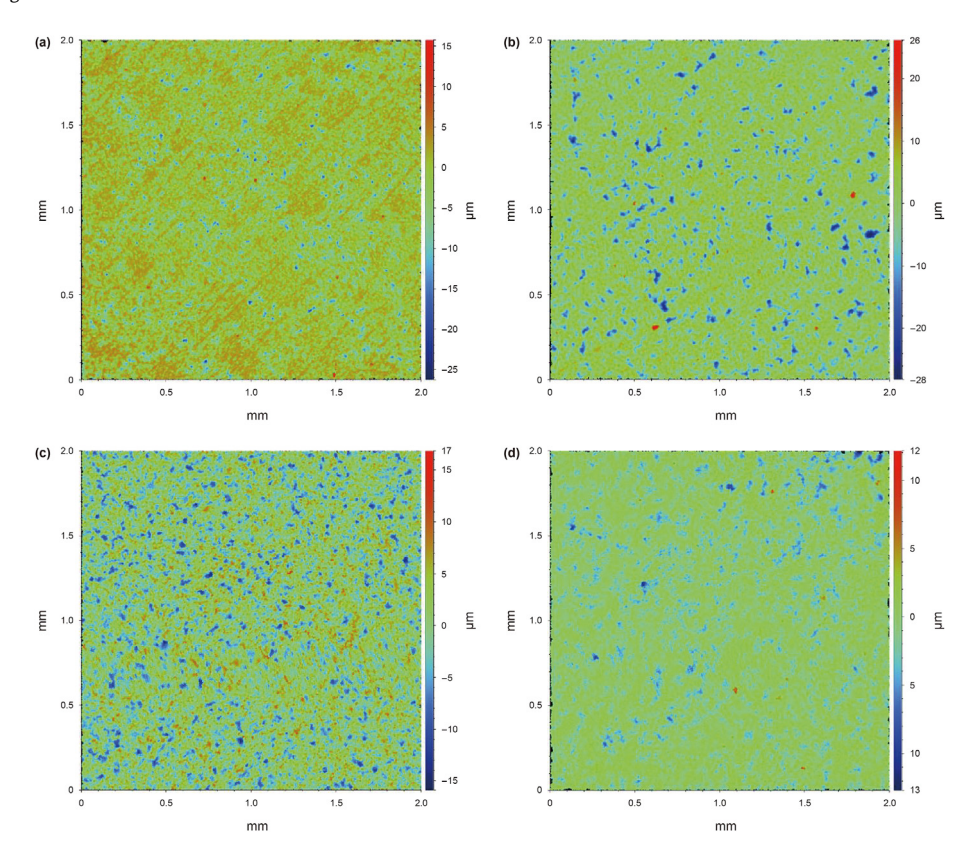


Fig. 11. Examples of profilometry images of (a) X65; (b) 1Cr; (c) 3Cr and (d) 5Cr steel surfaces after removal of corrosion products after 192 h of exposure.

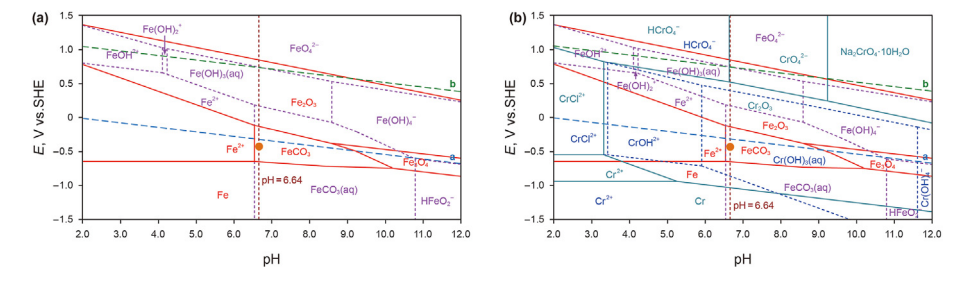


Fig. 12. Pourbaix diagrams for (a) Fe-H₂O-CO₂-Cl⁻ and (b) Fe-Cr-H₂O-CO₂-Cl⁻ systems in the CO₂-saturated solution at 60 °C and CO₂ partial pressure 0.8 bar.

$$Fe \to Fe^{2+}_{(aq)} + 2e^{-}$$
 (16)

$$Cr \to Cr_{(aq)}^{3+} + 3e^{-}$$
 (17)

Pourbaix diagrams were applied to identify the thermodynamically stable corrosion scales on the steel surfaces for the Fe–H₂O–CO₂–Cl⁻ and Fe–Cr–H₂O–CO₂–Cl⁻ systems. Fig. 12(a) illustrates the Pourbaix diagram for the Fe–H₂O–CO₂–Cl⁻ system at 60 °C and $p_{\rm CO_2}$ of 0.8 bar, where the red and purple lines represent solid and aqueous phases, respectively. Considering the initial solution pH of 6.64 and corrosion potential of –0.45 V/vs. SHE, the FeCO₃ is considered as the thermodynamically stable product with the coexisting products of FeCO₃(aq) ions in the aqueous phase. It should be noted that there is a difference for the pH value at steel surface and in bulk solution. Motte et al. (2018) used a mesh-based surface pH probe to monitor the pH value at carbon steel surface at 80 °C and pH of 6 and 6.6. Results indicated that the surface pH was higher than the bulk solution pH in all environments. At pH 6.6, the surface pH was approximately 0.5 higher than the bulk solution pH

during the 192 h of tests. Thus the surface pH in our tests should be higher than 6.64 which can be confirmed in Fig. 13, and the thermodynamically stable product is located in the FeCO₃ stable region. The formation reaction of FeCO₃ is:

$$Fe_{(aq)}^{2+} + CO_{3(aq)}^{2-} \rightarrow FeCO_{3(s)}$$
 (18)

The calculated Pourbaix diagram agreed with the XRD results in Fig. 5, where $FeCO_3$ was identified as the main corrosion products for X65 steel.

Figure 12(b) displays the Pourbaix diagram for the Fe–Cr– H_2O – CO_2 – CI^- system at 60 °C and p_{CO_2} of 0.8 bar. The thermodynamically stable corrosion products in this environment were FeCO₃ and Cr₂O₃ with FeCO_{3(aq)} and Cr(OH)_{3(aq)} in the aqueous phase. The results were in consistent with the XRD and Raman characterisations as shown in Figs. 5 and 6. The Cr(OH)₃ formation reaction of is described by:

$$\operatorname{Cr}_{(aq)}^{3+} + 3H_2O_{(l)} \to \operatorname{Cr}(OH)_{3(s)} + 3H_{(aq)}^+$$
 (19)

Cr(OH)₃ could be dehydrated and transformed into Cr₂O₃ as:

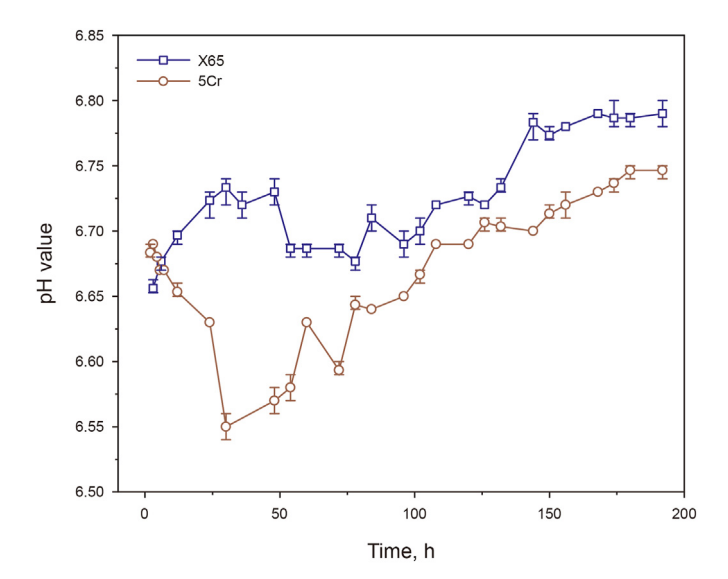


Fig. 13. Measured pH values of the solutions near X65 and 5Cr steel surfaces during 192 h of immersion tests.

$$2Cr(OH)_{3(s)} \rightarrow Cr_2O_{3(s)} + 3H_2O_{(1)}$$
 (20)

Guo et al. (2016) performed analysis on the inner layer formed on 3Cr steel at 80 °C and p_{CO_2} of 0.8 MPa, and the results demonstrated that the inner layer mainly contained FeCO₃ and Cr(OH)₃, and a very small amount of Cr₂O₃ may exist. The Cr₂O₃ was not identified on low-Cr steels in our study here which may be due to its low amount.

The Pourbaix diagram provides useful information for the thermodynamically stable corrosion products, however, the formation of crystalline FeCO₃ over a long exposure period is dominated by supersaturation and crystallisation kinetics, which is one of the limitations of the Pourbaix diagram. FeCO₃ tends to precipitate when the product of Fe²⁺ and CO₃²⁻ concentrations in the aqueous solution exceeds the solubility constant of FeCO₃ ($K_{\rm Sp,FeCO_3}$). The supersaturation of FeCO₃ ($S_{\rm FeCO_3}$) is described according to Eq. (21):

$$S_{\text{FeCO}_3} = \frac{c_{\text{Fe}^{2+}} c_{\text{CO}_3}^{2-}}{K_{\text{Sp.FeCO}_2}}$$
 (21)

where $c_{{\rm Fe}^{2+}}$ and $c_{{\rm CO_3}^{2-}}$ are the concentrations of ${\rm Fe}^{2+}$ and ${\rm CO}_3^{2-}$.

The pH value at steel surface has a significant effect on the formation kinetics of the corrosion products (De Motte et al., 2018). In our research, the pH values of the solution close to the steel surface were monitored to analyse the surface pH variations roughly. Fig. 13 illustrates the measured pH values of the solutions near X65 and 5Cr steel surfaces during 192 h of exposure. Clearly, the pH values of the solution near X65 surface were higher than those near 5Cr surface from 6 h to the end of the immersion tests. For the solution near X65 surface, the pH increased from 6.66 at the beginning to 6.73 at 30 h, then reduced to 6.68 at 80 h, after which maintained at 6.78 after 140 h. By contrast, for the electrolyte near 5Cr surface, the pH reduced significantly from 6.68 at the start to 6.55 at 30 h, then rose steadily to 6.75 after 192 h.

For X65 carbon steel, the pH value was influenced by both the hydrogen evolution reaction and the precipitation of FeCO₃. During the corrosion process, Fe^{2+} and the equivalent amount of alkalinity are released as indicated in Eq. (22) (Dugstad, 1998), resulting in a pH increase:

$$Fe_{(s)} + 2H_2CO_{3(aq)} \rightarrow Fe_{(aq)}^{2+} + 2HCO_{3(aq)}^{-} + H_{2(g)} \tag{22} \label{eq:22}$$

On the other hand, as shown in Eq. (18), the FeCO₃ precipitation consumes CO_3^{2-} , leading to H_2CO_3 dissociating equivalent amount of H⁺ to reduce the pH. As a result, the pH at the steel surface is determined by both the corrosion rate and the FeCO₃ precipitation rate, and the pH increases when the dissolution rate is faster than the rate of the FeCO₃ precipitation. For the first 30 h of immersion, the corrosion rate of X65 steel was relatively high from LPR results, and the steel surface was partially covered with FeCO₃ crystals from SEM images, suggesting that the corrosion rate played a leading role on pH, thus the pH near steel surface increased. After then, the precipitation of FeCO₃ came into prominence, leading to a pH reduction. With the consumption of Fe²⁺ and decrease in corrosion rate, the precipitation rate of FeCO₃ reduced, resulting in a rise in pH value again. From 140 h, the FeCO₃ corrosion products provided enough protection for the steel substrate, and both the corrosion rate and FeCO₃ precipitation rate were low. Dugstad (1998) also reported that the pH became constant when the precipitation rate equalled to corrosion rate of steel substrate.

For 5Cr steel, the initial corrosion rate was relatively low compared with X65 carbon steel for the first 30 h of exposure, and no crystalline FeCO₃ was identified from both SEM images and XRD results, suggesting a negligible effect of FeCO₃ precipitation. However, as indicated in the polarisation curves from Fig. 7(a), the Cr(OH)₃ layer was formed on 5Cr steel surface at the initial period which led to a notable prepassivation, resulting in a pH reduction according to Eq. (19). Therefore, the decline of pH at the initial 30 h for 5Cr steel was mainly attributed to formation of Cr(OH)₃ layer. After 30 h, the precipitation rate of Cr(OH)₃ reduced and the FeCO₃ formation was only limited, while the corrosion rate kept almost constant from beginning, leading to a steady increase in pH value.

According to the previous research (Guo et al., 2012), the pH reduction near steel surface can increase the critical supersaturatation (S_c) of FeCO₃, and nucleation rate is almost zero below S_c . From the measured near-surface pH, the pH near 5Cr surface was lower particularly at the period from 6 h to 72 h, indicating the 5Cr surface can delay the precipitation of FeCO₃ due to a large S_c .

Thus the effects of Cr content on the formation kinetics of corrosion products can be explained. For X65 and 1Cr steels, the crystalline FeCO₃ formed on the surfaces at a very similar time (6 h). According to the LPR results in Fig. 1, 3Cr and 5Cr steels provided slower releases of Fe²⁺ from the steel surface at the early stage compared to that of X65 and 1Cr steels. Referring to Eq. (21), the $K_{
m sp,FeCO_3}$ is mainly determined by the temperature, while the $c_{
m Fe^{2+}}$ was lower at 3Cr and 5Cr steel surfaces, leading to a lower S_{FeCO₃} for 3Cr and 5Cr. Moreover, the S_c values for 3Cr and 5Cr were higher due to the low near-surface pH, indicating that a high S_{FeCO_2} was required to achieve a rapid nucleation rate. Therefore, it requires a longer period to reach the S_c values for 3Cr and 5Cr steels, resulting in the development of less crystalline FeCO₃ on the surfaces. For 3Cr and 5Cr steels, more Cr³⁺ ions were dissolved from the substrate with immersion time, contributing to the formation of the Cr(OH)₃ layers based on reaction (19). Fig. 14 displays the schematic diagrams of the evolution of the corrosion products on X65 carbon steel and 5Cr steel.

4.2. Effect of Cr content and immersion time on the general and localised corrosion behaviours

Figure 15 shows the $1/R_p$ values together with the localised corrosion rates of different steels at various immersion times. Both general and localised corrosion rates of X65 and 1Cr steels decreased significantly with immersion times, while those of 3Cr

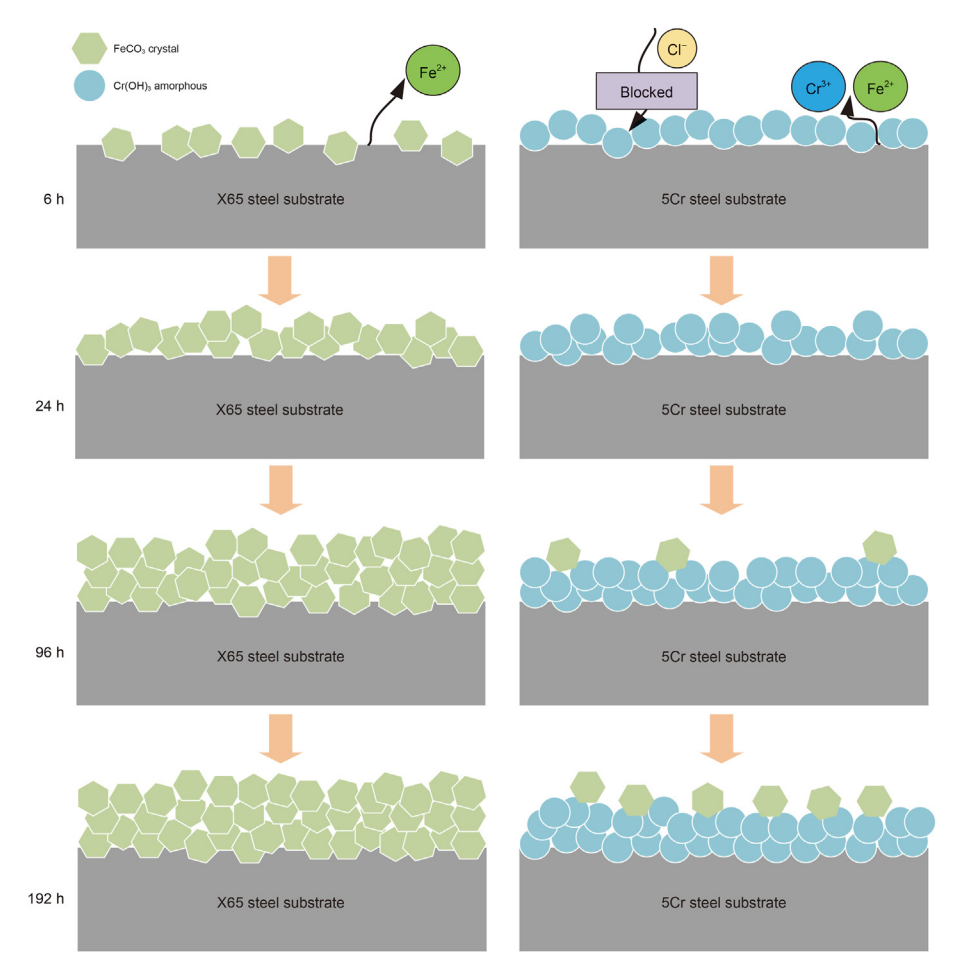


Fig. 14. Schematic diagrams of the formation and evolution of the corrosion products on X65 and 5Cr steels.

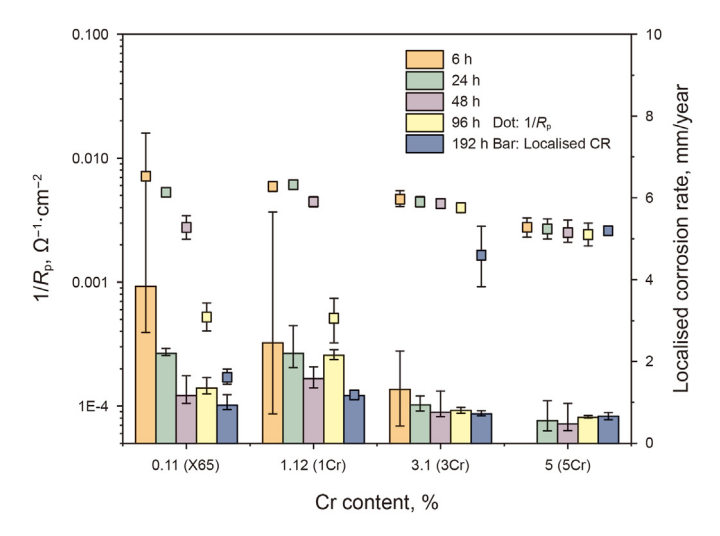


Fig. 15. Effects of Cr content and exposure time on the general and localised corrosion resistance of the steels.

reduced slightly and the corrosion behaviours of 5Cr were almost constant over 192 h. Moreover, 3Cr and 5Cr exhibit better general corrosion resistance at the initial period, while X65 and 1Cr show superior general corrosion resistance after 96 h. However, the localised corrosion rates of X65 and 1Cr were higher than that of 3Cr and 5Cr during 192 h of immersion, indicating that the crystalline FeCO₃ on X65 and 1Cr surfaces provided insufficient

localised corrosion protection.

At the initial corrosion period, the superior general and localised corrosion resistance of 3Cr and 5Cr are attributed to the prepassivation. As shown in Fig. 7(a), the addition of 3%Cr or more Cr content can maintain the steel surface in an obvious prepassive state compared with 1Cr and X65. According to the previous study (Wang et al., 2016), a spontaneous prepassivation was achieved for 3Cr and 5Cr at the early corrosion stage due to the formation of Cr(OH)3. However, the Cr contents in 1Cr and X65 steels were insufficient for the Cr(OH)₃ formation, and the precipitation of the FeCO₃ layers can provide poor protection. Therefore, as a diffusion barrier, the Cr(OH)3 film provided better general corrosion protection for 3Cr and 5Cr at the initial corrosion stage. It should be noted that 3%Cr becomes a critical Cr content in our corrosion environments to provide an adequate amount of Cr for the formation of Cr(OH)3, which then leads to a prepassivation characteristic, resulting in a superior corrosion resistance at the early stage.

Furthermore, the $Cr(OH)_3$ layer has the capability of cation selectivity and can block anions such as Cl^- penetrating the corrosion products (Chen et al., 2005). Previous studies suggest that Cl^- contributes to the catalytic dissolution of Fe substrate, film breakdown, and diffusion within the occluded cavity, thus aggravating the localised corrosion (Zhang et al., 2019). As a result, $Cr(OH)_3$ offered superior localised corrosion protection for the 3Cr and 5Cr steels.

However, as the corrosion products developed, the dense and compact crystalline FeCO₃ layer formed on X65 and 1Cr offered better general corrosion protection than the double-structural

corrosion product layers on 3Cr and 5Cr. The compact crystalline FeCO₃ layer on X65 and 1Cr can protect the steel surface by blocking the surface and acting as a diffusion barrier to reduce the general corrosion. However, the compact FeCO₃ layer on X65 and 1Cr cannot completely block the steel surfaces (Wang et al., 2022), and there were S_a available for the corrosion process as shown in the calculated S_a in Fig. 9(c). Thus localised attacks continued growing at S_a , suggesting that the FeCO₃ layer on X65 and 1Cr cannot offer enough protection against localised attacks.

5. Conclusions

In this study, the general and localised corrosion behaviours of X65, 1Cr, 3Cr and 5Cr steel as well as the formation and evolution of the corrosion products in CO₂ environments were investigated. The results show that the general and localised corrosion behaviours of different materials are closely related to the corrosion product formation and development. The addition of Cr contents in the steel suppressed both the general and localised corrosion attacks at the early corrosion stage. However, with the evolution of the corrosion products, the dense and compact crystalline FeCO₃ corrosion products were observed on X65 and 1Cr surfaces, reducing the general corrosion rates significantly; while the double corrosion product layers on 3Cr and 5Cr steels could significantly suppress localised corrosion but was unable to provide enough corrosion resistance for general corrosion over a long duration. The 3%Cr becomes a critical Cr content in our test environments to provide an adequate amount of Cr for the formation of Cr(OH)3 at the early stage, which then leads to a prepassivation characteristic, resulting in a superior general and localised corrosion resistance.

Declaration of competing interest

The authors declare that they have no known competing financial interests or personal relationships that could have appeared to influence the work reported in this paper.

Acknowledgements

This research is supported by the National Key R&D Program of China (2021YFB4001601), the Natural Science Foundation of Shandong Province (ZR2021QE036), the Fundamental Research Funds for the Central Universities (22CX06052A), the Postgraduate Innovation Funding Project of China University of Petroleum (East China) (YCX2020070), the Fundamental Research Funds for the Central Universities (20CX02405A) and the Development Fund of Shandong Key Laboratory of Oil & Gas Storage and Transportation Safety.

Appendix A. Supplementary data

Supplementary data to this article can be found online at https://doi.org/10.1016/j.petsci.2022.11.016.

References

- Ajayi, T., Gomes, J.S., Bera, A., 2019. A review of CO_2 storage in geological formations emphasizing modeling, monitoring and capacity estimation approaches. Petrol. Sci. 16 (5), 1028-1063. https://doi.org/10.1007/s12182-019-0340-8.
- ASTM, Standard G1-03, 2003a. Standard Practice for Preparing, Cleaning, and Evaluating Corrosion Test Specimens. ASTM International, West Conshohocken, PA.
- ASTM, Standard G46-94, 2003b. Standard Guide for Examination and Evaluation of Pitting Corrosion. ASTM International, West Conshohocken, PA.
- Bai, Z.Q., Chen, C.F., Lu, M.X., et al., 2006. Analysis of EIS characteristics of CO₂ corrosion of well tube steels with corrosion scales. Appl. Surf. Sci. 252 (20), 7578–7584. https://doi.org/10.1016/j.apsusc.2005.09.011.

Brug, G.J., van, d.E.A., Sluyters-Rehbach, M., et al., 1984. The analysis of electrode impedances complicated by the presence of a constant phase element. J. Electroanal. Chem. 176 (1–2), 275–295. https://doi.org/10.1016/S0022-0728(84)80324-1.

- Carvalho, D.S., Joia, C.J.B., Mattos, O.R., 2005. Corrosion rate of iron and iron-chromium alloys in CO₂ medium. Corrosion Sci. 47 (12), 2974–2986. https://doi.org/10.1016/j.corsci.2005.05.052.
- Chen, C.F., Lu, M.X., Sun, D.B., et al., 2005. Effect of chromium on the pitting resistance of oil tube steel in a carbon dioxide corrosion system. Corrosion 61 (6), 594–601. https://doi.org/10.5006/1.3278195.
- Chen, L., Dong, B., Liu, W., et al., 2022. Failure analysis of corrosion products formed during CO₂ pre-corrosion of X70 and 3Cr steels: effect of oxygen contamination. Eng. Fail. Anal. 140, 106529. https://doi.org/10.1016/j.engfailanal.2022.106529.
- Cui, G., Li, Z.L., Yang, C., et al., 2016. The influence of DC stray current on pipeline corrosion. Petrol. Sci. 13 (1), 135–145. https://doi.org/10.1007/s12182-015-0064-3.
 Dugstad, A., 1998. Mechanism of Protective Film Formation during CO₂ Corrosion of Carbon Steel, vol. 98. CORROSION. Houston. Texas.
- Gu, S., Li, Y., Teng, L., et al., 2019. An experimental study on the flow characteristics during the leakage of high pressure CO₂ pipelines. Process Saf. Environ. Protect. 125, 92–101. https://doi.org/10.1016/j.psep.2019.03.010.
- Guo, S., Xu, L., Zhang, L., et al., 2016. Characterization of corrosion scale formed on 3Cr steel in CO₂-saturated formation water. Corrosion Sci. 110, 123–133. https://doi.org/10.1016/j.corsci.2016.04.033.
- Guo, S., Xu, L., Zhang, L., et al., 2012. Corrosion of alloy steels containing 2% chromium in CO₂ environments. Corrosion Sci. 63, 246–258. https://doi.org/10.1016/j.corsci.2012.06.006.
- Hua, Y., Barker, R., Charpentier, T., et al., 2015. Relating iron carbonate morphology to corrosion characteristics for water-saturated supercritical CO₂ systems. J. Supercrit. Fluids 98, 183—193. https://doi.org/10.1016/j.supflu.2014.12.009.
- Hua, Y., Barker, R., Neville, A., 2014. Effect of temperature on the critical water content for general and localised corrosion of X65 carbon steel in the transport of supercritical CO₂. Int. J. Greenh. Gas Control 31, 48–60. https://doi.org/ 10.1016/i.ijggc.2014.09.026.
- Hua, Y., Mohammed, S., Barker, R., et al., 2020. Comparisons of corrosion behaviour for X65 and low Cr steels in high pressure CO₂-saturated brine. J. Mater. Sci. Technol. 41, 21–32. https://doi.org/10.1016/j.jmst.2019.08.050.
- Hua, Y., Shamsa, A., Barker, R., et al., 2018. Protectiveness, morphology and composition of corrosion products formed on carbon steel in the presence of Cl⁻, Ca²⁺ and Mg²⁺ in high pressure CO₂ environments. Appl. Surf. Sci. 455, 667–682. https://doi.org/10.1016/j.apsusc.2018.05.140.
- Jiang, K., Ashworth, P., 2021. The development of Carbon Capture Utilization and Storage (CCUS) research in China: a bibliometric perspective. Renew. Sustain. Energy Rev. 138, 110521. https://doi.org/10.1016/j.rser.2020.110521.
- Kermani, M.B., Morshed, A., 2003. Carbon dioxide corrosion in oil and gas production-A compendium. Corrosion 59 (8), 659–683. https://doi.org/ 10.5006/1.3277596.
- Li, P., Tan, T.C., Lee, J.Y., 1996. Impedance spectra of the anodic dissolution of mild steel in sulfuric acid. Corrosion Sci. 38 (11), 1935—1955. https://doi.org/10.1016/S0010-938X(96)00079-0.
- Li, W., Xu, L., Qiao, L., et al., 2017. Effect of free Cr content on corrosion behavior of 3Cr steels in a CO₂ environment. Appl. Surf. Sci. 425, 32–45. https://doi.org/10.1016/j.apsusc.2017.06.320.
- Li, Y., Liu, X., Wang, C., et al., 2020. Research progress on corrosion behavior of gaseous CO₂ transportation pipelines containing impurities. Acta Metall. Sin. 57 (3), 283–294. https://doi.org/10.11900/0412.1961.2020.00165.
- Macdonald, D.D., Scott, A.C., Wentrcek, P., 1979. External reference electrodes for use in high temperature aqueous systems. J. Electrochem. Soc. 126 (6), 908–911. https://doi.org/10.1149/1.2129192.
- Motte, R., Basilico, E., Mingant, R., et al., 2020. A study by electrochemical impedance spectroscopy and surface analysis of corrosion product layers formed during CO₂ corrosion of low alloy steel. Corrosion Sci. 172, 108666. https://doi.org/10.1016/j.corsci.2020.108666.
- Motte, R., Mingant, R., Kittel, J., et al., 2018. Near surface pH measurements in aqueous CO₂ corrosion. Electrochim. Acta 290, 605–615. https://doi.org/ 10.1016/j.electacta.2018.09.117.
- Nesic, S., 2012. Effects of multiphase flow on internal CO₂ corrosion of mild steel pipelines. Energy Fuel. 26 (7), 4098–4111. https://doi.org/10.1021/ef3002795.
- OLI Systems. Inc, OLI analyzer studio, Vers.3.1, 108 American road, morris plaines. New Jersey. www.olisystems.com.
- Sharifzadeh, M., Triulzi, G., Magee, C.L., 2019. Quantification of technological progress in greenhouse gas (GHG) capture and mitigation using patent data. Energy Environ. Sci. 12 (9), 2789–2805. https://doi.org/10.1039/c9ee01526d.
- Sun, B., Zuo, X., Cheng, X., et al., 2020. The role of chromium content in the long-term atmospheric corrosion process. npj Mater. Degrad. 4 (1), 1–9. https://doi.org/10.1038/s41529-020-00142-5.
- Sun, M., Du, C., Liu, Z., et al., 2021. Fundamental understanding on the effect of Cr on corrosion resistance of weathering steel in simulated tropical marine atmosphere. Corrosion Sci. 186, 109427. https://doi.org/10.1016/j.corsci.2021.109427.
- Takabe, H., Ueda, M., 2001. The Formation Behavior of Corrosion Protective Films of Low Cr Bearing Steels in CO₂ Environments. CORROSION 2001, Houston, Texas.
- Wang, B., Xu, L., Zhu, J., et al., 2016. Observation and analysis of pseudopassive film on 6.5%Cr steel in CO₂ corrosion environment. Corrosion Sci. 111, 711–719. https://doi.org/10.1016/j.corsci.2016.06.006.
- Wang, C., Hua, Y., Nadimi, S., et al., 2022. Anti-corrosion characteristics of FeCO₃ and Fe_xCa_yMg_zCO₃ scales on carbon steel in high-PT CO₂ environments. Chem. Eng.

- J. 431, 133484. https://doi.org/10.1016/j.cej.2021.133484.
- Wang, C., Hua, Y., Nadimi, S., et al., 2021. Determination of thickness and air-void distribution within the iron carbonate layers using X-ray computed tomography. Corrosion Sci. 179, 109153. https://doi.org/10.1016/j.corsci.2020.109153.
- Wang, C., Li, Y., Teng, L., et al., 2019. Experimental study on dispersion behavior during the leakage of high pressure CO₂ pipelines. Exp. Therm. Fluid Sci. 105, 77–84. https://doi.org/10.1016/j.expthermflusci.2019.03.014.
- Xie, Y., Xu, L., Gao, C., et al., 2012. Corrosion behavior of novel 3%Cr pipeline steel in CO₂ Top-of-Line Corrosion environment. Mater. Des. 36, 54–57. https://doi.org/ 10.1016/j.matdes.2011.11.003.
- Xu, L., Guo, S., Chang, W., et al., 2013. Corrosion of Cr bearing low alloy pipeline steel in CO₂ environment at static and flowing conditions. Appl. Surf. Sci. 270, 395–404. https://doi.org/10.1016/j.apsusc.2013.01.036.
- Xu, L., Wang, B., Zhu, J., et al., 2016. Effect of Cr content on the corrosion performance of low-Cr alloy steel in a CO₂ environment. Appl. Surf. Sci. 379, 39–46. https://doi.org/10.1016/j.apsusc.2016.04.049.
- Xu, Z.X., Li, S.Y., Li, B.F., et al., 2020. A review of development methods and EOR

- technologies for carbonate reservoirs. Petrol. Sci. 17 (4), 990–1013. https://doi.org/10.1007/s12182-020-00467-5.
- Yan, X., Long, A., Liang, H., et al., 2015. Ecological features of sulphate-reducing bacteria in a CO₂ flooding gathering environment. J. Nat. Gas Sci. Eng. 22, 335–339. https://doi.org/10.1016/j.jngse.2014.09.019.
- Yang, L.S., Yang, C., et al., 2021. Effect of anodic dissolution and passivation on X80 steel in NaHCO₃ solution. Petrol. Sci. 18 (1), 285–294. https://doi.org/10.1007/s12182-020-00532-z.
- Zhang, S., Hou, L., Du, H., et al., 2019. Synergistic contribution of chloride and bicarbonate ions to pitting corrosion behavior of carbon steel. Corrosion 75 (9), 1034–1043. https://doi.org/10.5006/3195.
- Zhao, Y., Liu, W., Fan, Y., et al., 2020. Effect of Cr content on the passivation behavior of Cr alloy steel in a CO₂ aqueous environment containing silty sand. Corrosion Sci. 168, 108591. https://doi.org/10.1016/j.corsci.2020.108591.
- Zhu, J., Xu, L., Lu, M., 2015. Electrochemical impedance spectroscopy study of the corrosion of 3Cr pipeline steel in simulated CO₂-saturated oilfield formation waters. Corrosion 71 (7), 854–864. https://doi.org/10.5006/1494.